JOURNAL OF AIRCRAFT
Vol. 61, No. 4, July–August 2024

Numerical Icing Simulations of Cylindrical Geometry and Comparisons to Flight Test Results

Zachary R. Milani,* Edgar Matida,† Fatemeh Razavi,‡ Kaniz Ronak Sultana,§ and R. Timothy Patterson¶
Carleton University, Ottawa, Ontario K1S 5B6, Canada
and
Leonid Nichman,** Ali Benmeddour,†† and Kenny Bala‡‡
National Research Council of Canada, Ottawa, Ontario K1 V 1J8, Canada

https://doi.org/10.2514/1.C037682

There is growing interest in government and industry to use numerical simulations for the Certification by Analysis of aircraft ice protection systems as a cheaper and more sustainable alternative to wind-tunnel and flight testing. The ice accretion on a cylindrical test article mounted under the wing of the National Research Council of Canada's Convair-580 research aircraft during a flight test in Appendix O icing conditions was simulated using Ansys FENSAP-ICE™. A multishot simulation with input parameters averaged over the full icing period led to an increased level of liquid catch and ice accretion (by mass), and a broader ice profile when compared to a simulation with shot-averaged input parameters. An additional simulation using Ansys' proprietary "extended icing data with vapor solution" method for calculating heat fluxes at the icing surface resulted in a broader ice profile in comparison to the classical technique, which produced a similar amount of accretion by mass. No combination of simulation settings, input parameters, and multishot methods tested in this study generated the same level of surface detail observed during flight testing, however, the amount of ice accretion, general location of ice features, and formation processes were in good agreement with the experimental results.

Nomenclature

c_h	=	convective heat-transfer coefficient, $W \times m^{-2} \times K^{-1}$
c_p	=	specific heat, $J \times kg^{-1} \times K^{-1}$
e_d	=	energy of droplet
h	=	thickness, m
L	=	latent heat, $J \times kg^{-1}$
LWC	=	liquid water content, $kg \times m^{-3}$
$\dot{m}$	=	mass transfer rate, $k \times s^{-1}$
q	=	heat flux, $W \times m^{-2}$
$\boldsymbol{T}$	=	temperature, K
t	=	time, s
$\bar{V}$	=	velocity mean, $m \times s^{-1}$
$\boldsymbol{V}$	=	velocity vector, $m \times s^{-1}$
β	=	collection efficiency
ε	=	solid emissivity
ρ	=	density, $kg \times m^{-3}$
σ	=	Boltzmann constant, $W \times m^{-1} \times K^{-4}$
$\vec{\nabla}$	=	gradient operator of vector field

Subscripts

d	=	droplet
evap	=	evaporation
f	=	water film
rec	=	recovery
∞	=	reference (freestream)

I. Introduction

IN-FLIGHT ice accretion is a significant safety concern to the modern aviation industry, with an icing-related accident occurring in North America as recently as 2022 [1–7]. Aircraft that travel through regions of supercooled clouds risk accreting ice on important airframe surfaces and critical flight data sensors [8]. Ice formation on the leading edge of wings and important control surfaces can cause the aircraft to experience a reduction in lift, increase in drag, and deteriorated flight performance that can lead to loss of control [9]. Pilots rely on information provided by aircraft in-situ sensors, weather radar, weather advisories, pilot reports, and advanced forecasting algorithms to identify icing conditions along their flight path. Intended flight through known or forecasted icing conditions is possible as long as the aircraft has an ice protection system (IPS) that has been certified specifically for those hazardous conditions. The development and certification process of an IPS can be costly, time consuming, and sometimes dangerous with flight testing in natural icing conditions. This has led to a growing appetite in industry and government for Certification by Analysis (CbA) using numerical simulations [10]. Access to reliable ice modeling tools is extremely important, given that severe weather events, particularly those that can be hazardous for air travel, are expected to increase in frequency and severity due to the global rise in temperature and humidity [11,12].

Fatal aviation accidents such as those described in Ref. [4], and years of ice accretion research, have led major air transportation authorities to recognize two main definitions of hazardous airframe icing conditions: Appendix C conditions, which describe small

Received 25 August 2023; revision received 14 February 2024; accepted for publication 20 February 2024; published online Open Access 19 March 2024.

*Ph.D. Student, Department of Mechanical and Aerospace Engineering and Department of Earth Sciences; ZacharyMilani@cmail.carleton.ca (Corresponding Author).
†Full Professor, Department of Mechanical and Aerospace Engineering; Edgar. Matida@carleton.ca.
‡Postdoctoral Fellow, Department of Mechanical and Aerospace Engineering; FatemehRazavi@cunet.carleton.ca.
§Postdoctoral Fellow, Department of Mechanical and Aerospace Engineering; KanizRonakSultana@cunet.carleton.ca.
¶Chair and Full Professor, Department of Earth Sciences; Tim.Patterson@carleton.ca.
**Senior Research Officer, Flight Research Laboratory; Leonid.Nichman@nrc-cnrc.gc.ca; also Adjunct Professor, Department of Earth Sciences, Carleton University.
††Senior Research Officer, Aerodynamics Laboratory; Ali.Benmeddour@nrc-cnrc.gc.ca.
‡‡Research Council Officer, Flight Research Laboratory; Kliti.Bala@nrc-cnrc.gc.ca.

droplets; and Appendix O conditions, which focus on supercooled large droplets (SLD) [13,14]. SLD conditions are particularly dangerous because large droplets have been shown to move impingement limits farther downstream (potentially aft of IPS) while also increasing the global and local liquid catch efficiencies, thereby leading to more ice accretion, assuming other icing parameters [temperature, velocity, liquid water content (LWC), etc.] are the same [15]. Regulations indicate that aircraft intending to fly through known icing conditions must be equipped with an IPS that prevents ice buildup from reducing flight performance beyond safe standards. Common IPS systems used by commercial aircraft to protect against surface icing include bleed air from the engines, electrothermal heaters, electromechanical devices, pneumatic boots, and weeping fluid systems [16]. Determining aircraft tolerances and ice-accretion shapes in these icing conditions (with and without IPS) often involves numerical simulations for preliminary analysis of the aircraft and IPS, icing wind-tunnel experiments for verification of numerical simulations and IPS testing, and flight testing in natural conditions for final validation and certification. With comprehensive numerical simulation packages, it may be possible to reduce the need for the expensive wind-tunnel experiments and dangerous flight testing that are currently necessary for IPS certification [17].

Ansys FENSAP-ICE [18–20] is a well-known and commercially available numerical ice-accretion simulation package that models three-dimensional (3-D) ice shapes and has IPS modeling capabilities. LEWICE3D [21] is another well-established icing simulation package, available only in the United States and to other authorized users. There are, however, numerous in-house software packages that exist at the time of publishing that are not openly accessible to the general public, e.g., The National Research Council of Canada (NRC) Morphogenetic Code [22], IGLOO3D [23,24], PoliMIce [25,26], SIMBA/MESS3D [27], and ONICE3D [28,29]. In general, modern simulation packages will often produce acceptable estimates of rime ice shapes in two-dimensional (2-D) and 3-D but less so in glaze ice conditions in 3-D. Glaze ice models are more complex because they require heat- and mass-transfer calculations for the liquid film on the icing surface, whereas rime ice models assume droplets freeze on impact. Typically, the procedure for simulating ice accretion includes: 1) a flow model using a Reynolds Averaged Navier Stokes solver, 2) droplet tracking and deposition using a Eulerian or Lagrangian framework, 3) mass and energy balance on the icing surface using a Messinger or stochastic model, and 4) calculation of surface displacement due to ice accretion. In practice, ever-evolving ice shapes are constantly transforming the aerodynamic and droplet impingement characteristics of the icing surface. Steady-state numerical simulations account for this transient behavior by using a multishot approach [19] that breaks the icing period into temporal segments, where surface displacement is calculated (i.e., Steps 1 through 4) and the original grid is remeshed or morphed prior to the next shot [20]. The multishot approach with automatic remeshing is a common method for simulating glaze ice on 3-D geometries and has its own module in Ansys FENSAP-ICE™.

Ice shapes generated by numerical simulations must be compared against experimental data that is often produced by running wind-tunnel experiments [30]. Wind-tunnel testing is an extremely useful and necessary validation tool for airframe icing. The ability to control the icing environment within an icing wind tunnel provides the opportunity to investigate fundamental icing processes and the aerodynamic penalties caused by ice accretion on certain parts of the airframe. However, the hazardous icing conditions that are recreated during wind-tunnel testing are a simulation of the natural icing environment. Certain inimitable atmospheric conditions, such as those involving large hydrometeors as described in Appendix O, are particularly difficult to simulate in wind tunnels. For instance, SLD are subject to gravitational settling and have difficulty reaching low-set temperatures and steady-state conditions before impact because of their nonfreezing source temperatures and their significant thermal mass. Also, liquid droplets have a different impact orientation and geometry in horizontal and vertical flow tunnels, unlike in the natural vertical precipitation and perpendicular lateral impact. In a mixed-phase icing environment, natural complex ice-crystal shapes are even more difficult to generate artificially. Therefore, in addition to wind-tunnel experiments, there is also a need to further explore flight-test accreted-ice shapes collected in natural icing conditions. The atmospheric data collected during flight testing can produce well-defined characterizations of natural icing conditions so that detailed sets of input parameters can be generated for numerical icing simulations, whereas the accreted-ice shapes collected in those conditions can be used to validate the simulation results. This combination of data can help to advance numerical techniques by ensuring simulations can produce ice shapes that are authentic to true natural icing conditions (as opposed to being authentic to icing wind-tunnel conditions). To the authors' knowledge, Ref. [31] is the most recent study attempting to validate numerical simulations using flight-test ice shapes they collected, and Ref. [32] is an example of similar studies that focus on gathering different flight-test ice shapes for verification of wind-tunnel experiments. Given the growing interest in CbA, the versatile multishot with automatic remeshing approach to ice accretion modeling, and the capabilities of advanced atmospheric-research aircraft and instruments [33], it is important to reassess the viability of numerical simulation technology using data obtained through flight tests in natural icing conditions.

This study investigates the ability of Ansys FENSAP-ICE to model ice accretion during flight tests in natural icing conditions using data obtained onboard the NRC Convair-580 research aircraft. The NRC Convair-580 is equipped with state-of-the-art instruments and probes, which provide a detailed characterization of local atmospheric icing conditions. The first-generation Platform for Ice-accretion and Coatings Tests with Ultrasonic Readings (PICTUR) [33] was installed on the aircraft for studies of natural ice accretion. The PICTUR features cylindrical test articles with subsurface electrothermal heaters to test anti- and deicing procedures. Cylinders have been used to study important ice accretion processes [34] and the capabilities of numerical icing software [22,35]. Cylindrical geometries can be found on airframe structures, aircraft probes and sensors, and even the hangar cables that support suspension bridges. A single ∼10-min ice-accretion period consistent with Appendix O conditions was identified during a research flight over the St. Lawrence region of southwestern Quebec in March of 2022, which was part of the Winter Precipitation Type Research Multi-Scale Experiment (WINTRE-MIX) campaign [36] that targeted intensive near-freezing precipitation events. Data from the icing period was parameterized and input into Ansys FENSAP-ICE, where the multishot remeshing method was used to simulate ice accretion on the cylinders of the PICTUR, with the goal of matching the experimental results.

II. Airborne Methods

The PICTUR has a symmetrical, cross-shaped design, which is mounted on a pylon located under the wing of the NRC Convair-580 research aircraft (see Fig. 1). The PICTUR is mounted such that its two cylindrical test articles (these make up the cross shape) are oriented perpendicular to the direction of travel and fully exposed, without obstruction, to the atmospheric conditions and icing environment. The cylinders are oriented at a 45-deg angle relative to the horizontal plane of the aircraft, due to spatial integration constraints.

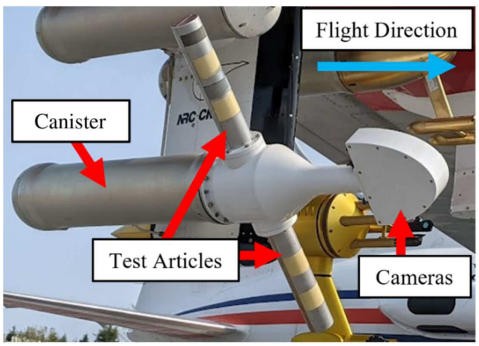

Fig. 1 Labeled schematic of the PICTUR mounted on a starboard pylon under the wing of the NRC Convair-580 aircraft.

The test articles, made from aluminum, are 63.5 mm in diameter. High-temperature electrothermal heating pads are installed on the inside of the leading-edge surface. The heating pads are used to evaluate active ice-protection solutions with the added capability of resetting the test articles by shedding ice in between icing periods. The PICTUR also contains an experimental ultrasonic ice-accretion sensor (NRC UIAS) [37], developed in-house, to determine the instance when ice accretion begins. This version of the UIAS sensor can detect the accretion of the ice layer but not the thickness of the accreted ice. Two cameras with light-emitting-diode lights are installed at the front of the probe to monitor ice accretion on the test articles during flight tests and provide qualitative visuals of ice formation over time.

The PICTUR is one of the many probes and sensors onboard the NRC Convair-580 airborne laboratory, which is a heavily modified twin engine turbo-prop aircraft capable of performing airborne measurements of atmospheric properties related to severe weather and icing events [38,39]. The atmospheric properties measured by the aircraft include atmospheric state, aircraft state, aerosol and gas phase, and the single-particle and bulk microphysical properties of clouds. All probes and sensors used in this study are summarized in Table 1, and their locations are tagged in Supplementary Fig. S1; or go to the Supplemental Materials link that accompanies the electronic version of this article at http://arc.aiaa.org. The atmospheric and aircraft-state data are sampled at 1-Hz resolution and their $\pm\sigma$ measurement uncertainty estimates are summarized in Supplementary Table S1; or go to the Supplemental Materials link that accompanies the electronic version of this article at http://arc.aiaa.org (uncertainties are based on the documentation provided by Ref. [40]). The LWC and total water content measurements are collected at 1-Hz resolution using the Nevzorov hot-wire probe [41]. In acknowledging the challenges in quantifying the Nevzorov's uncertainty, especially when large hydrometeors are present [42,43], this study follows the lead of Refs. [38,44] in estimating a measurement uncertainty up to $\pm 0.05\ \mathrm{g \times m^{-3}}$, which is more conservative than other estimates provided in the literature (e.g., Ref. [45] estimates measurement uncertainty to be $\pm 0.02\ \mathrm{g \times m^{-3}}$).

Several imaging probes are required to investigate the full range of hydrometeor sizes present in the natural icing environment, which is critical for accurately classifying the icing envelope. The fast cloud droplet probe (FCDP, 5–50 μm) [46], 2-D stereo probe (2-DS, 10–1200 μm) [47], and high-volume precipitation spectrometer Ver. 3 (HVPS-3,150–19,200 μm) [48] are used to continuously image hydrometeors over a large size-range, spanning several orders of magnitude from ~2 to 19,200 μm in diameter. Hydrometeors are classified using an in-house convolutional neural network classification algorithm similar to Ref. [49]. Due to factors associated with image correction, particle reinjection, classification errors, and the combination of data from multiple sensors, the propagated uncertainty associated with particle sizing can grow to be within the range of 10%–100% [50]. The processed hydrometeor data are then used to produce an estimate of the time-resolved particle size distribution (PSD) and median volumetric diameter (MVD) for the icing period at 0.2-Hz resolution. The current classification algorithm is not yet fully capable of identifying the matter phase from the shape of the hydrometeors recorded in the particle images. This means the PSD and MVD data used to define simulation input parameters for liquid droplets may be biased toward larger values due to the presence of relatively large ice hydrometeors. For context, MVD is a core parameter used in icing simulations, and overestimating this value will typically lead to a greater collection efficiency, which produces a more conservative estimate of ice accretion.

Table 1 Summary of the scientific probes and sensors used in this study, the properties they measure, and their locations, as shown in Supplementary Fig. S1

Location	Property	Probe
4	Liquid and total water content	Nevzorov Hotwire Probe [41]
4, 6	Icing detection	Collins RID [54]
5	Static air pressure	Honeywell PPT2 Pressure Transducer
4	Static air temperature	Rosemount 102 Total Air Temperature Probe
2	Wind speed and direction	Rosemount 858 Air Data Probe
5	Aircraft speed, direction, orientation	KVH Inertial Navigation System (inside cabin)
2, 3, 8, 9	Imaging of hydrometeors	FCDP: 2–50 μm [46] 2-DS: 10–1200 μm [47] HVPS Ver. 3: 150–19, 200 μm [48]
2	Ice-accretion detection and measurement	PICTUR [33], UIAS [37]

III. The Icing Period

Interesting periods of ice accretion were identified in the data obtained by the NRC Convair-580 during the 2022 WINTRE-MIX campaign [36,40,51,52], which studied near-freezing precipitation near southern Quebec and northern New York. The icing period selected for analysis occurred during WINTRE-MIX flight 6 on March 6, 2022, in transit from Ottawa to the greater Montreal/Champlain Valley area. The icing period began when the NRC UIAS sensor was triggered at 13:20:21 (0 s in Fig. 2) and ended when the operator initiated the internal heaters at 13:30:12 (590 s in Fig. 2). The PICTUR was allowed to accrete ice for nearly 10 min while the Convair-580 traveled ~82 km through a local weather system at a constant altitude of ~3500 m and a mean true air speed of 92 $\mathrm{m \times s^{-1}}$.

A. The Flight-Test Icing Environment

The atmospheric properties relevant to ice accretion modeling are shown in Fig. 2. The longitudinal velocity (positive direction flowing from leading to trailing edge of cylinder), lateral velocity (positive direction flowing from cylinder tip to base), and vertical velocity

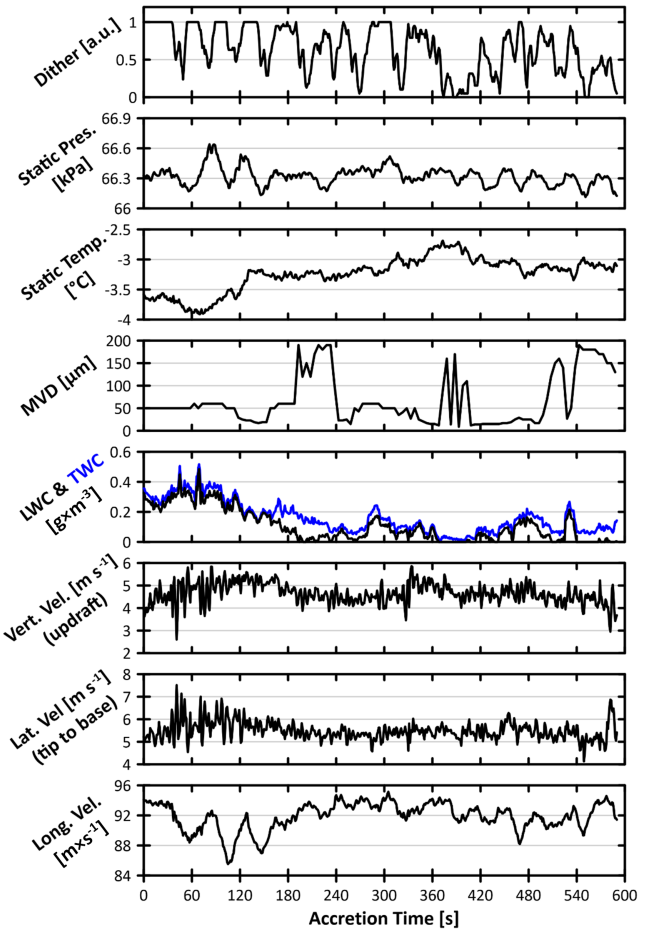

Fig. 2 Icing properties for the WINTRE-MIX F06 icing period.

(positive direction flowing upward) are computed from the perspective of the PICTUR probe and relative to the wind. These velocities are calculated by subtracting wind speed from aircraft inertial velocity to obtain the 3-D components of airspeed relative to the wind and translated into the perspective of the PICTUR using the aircraft pitch, roll, and heading. Prior to the 150-s mark is when LWC is at its highest and the static air temperature is at its lowest. Shortly after the 150-s mark the MVD increases abruptly, the nonliquid water content increases, and a noticeable decrease in the icing intensity is observed in the PICTUR video recording [53]. The normalized Dither signal produced by the Collins Rosemount Icing Detector (RID) is used as a qualitative indicator of icing intensity [54] to show high-intensity behavior (i.e., high-frequency oscillations with values reaching unity) during the first 150 s, which further suggests that atmospheric conditions were most conducive for ice accretion during this time. The four sets of timestamped hydrometeor images in Supplementary Fig. S2 (or go to the Supplemental Materials link that accompanies the electronic version of this article at http://arc.aiaa.org) were captured using the 2-DS probe and show the degree to which the hydrometeor population changes during the 10 minicing period. Moderately sized supercooled droplets (~50 μm) dominated the early period [53 s in Supplementary Fig. S3 (or go to the Supplemental Materials link that accompanies the electronic version of this article at http://arc.aiaa.org)]; liquid hydrometeors cycled between small and mixed-sized droplets in the middle period, where some ice hydrometeors were also imaged (210 and 337 s); and mixed-phase conditions including SLD (~180 μm) and various ice *habits* (i.e., ice-crystal shapes) were observed near the end period (541 s). The decrease in LWC and icing intensity in the PICTUR video, the relaxation of the normalized Dither signal, and the multimodal hydrometeor environment all illustrate how variability is intrinsic to natural ice accretion (in contrast to steady-state wind-tunnel experiments) and why careful consideration is necessary when simulating natural icing conditions.

To categorize the icing envelope of this icing period, the cumulative mass vs droplet diameter curve shown in Supplementary Fig. S3 was compared against the cumulative mass curves of all Appendix O icing envelopes; or go to the Supplemental Materials link that accompanies the electronic version of this article at http://arc.aiaa.org. The cumulative mass curve was produced by averaging the particle concentrations from the PSDs over the entire icing period, multiplying the average concentrations by their corresponding spherical droplet volumes (droplet density was assumed to be constant), and normalizing and summing the resulting curve. The 10-min icing period has an averaged MVD of 67 μm, a maximum droplet diameter >100 μm, and a trend that is bounded best by the "MVD >40 μm" and "MVD <40 μm" curves that define the Appendix O freezing drizzle standard.

B. The Flight-Test Accreted-Ice Shape

In general, aircraft can accrete two main types of ice during flight (or a mix of the two): rime ice and glaze ice. Rime ice occurs when impinging liquid droplets freeze on impact and tends to form when ambient temperature or LWC levels are low. Glaze ice forms when impinging liquid freezes more slowly on the icing surface and tends to form in warmer ambient temperatures or high LWC conditions [3]. The PICTUR video recording shows mostly clear glaze-ice accretion after exposure to the icing environment described in the preceding text. The accreted ice shape shows three distinct region types of glaze ice on the cylinder, which are discussed in [34]: the smooth, transition, and rough zones. The smooth zone in Fig. 3 covers an angular extent of ±~10 deg from the stagnation point and extends to the transition zone. The ice in the smooth zone is translucent and smooth except for the small, white surface features, which are most noticeable when multiphase conditions are observed by the particle-imaging probes. These features are assumed to be small ice hydrometeors that hit and stick or small droplets that partially freeze upon impact and contribute very little to the overall ice shape.

The smooth zone typically maintains a thin uniform film, which is due to the increased collection efficiency close to the stagnation point. This film allows for the liquid–solid interface to freeze slowly without trapping air pockets and produces a smooth ice surface. As aerodynamic forces push the film aft, surface tension causes the liquid to coalesce into beads, which may grow larger with droplet impingement or smaller if shear forces tear the liquid away from the surface. Beads that exist outside the stagnation zone are subjected to increased convective heat transfer due to the flow regime over the circular geometry. As the hemispherical-shaped beads freeze, the surface roughness and surface area at that location increases, which further increases the heat transfer and the collection efficiency in the region. These factors help to establish the rough zone, where protuberances grow relatively quickly, often creating a large horn structure, ridges, sizable roughness elements, and ice features such as nodules and ice feathers. The PICTUR video recording shows that the rough zone and sizable roughness elements such as those in Fig. 3 began forming early, within the first 3 minutes of the icing period.

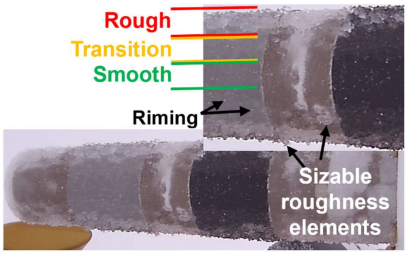

Fig. 3 Video snapshot of the sizable roughness elements in the rough and transition zones on the PICTUR cylinder at the 590-s mark of the WINTRE-MIX F06 icing period.

The intermediate region, or transition zone, existing between the smooth and rough zones, is defined by a distinct but moderate increase in surface roughness. Reference [55] determined that the location of the transition zone, at least initially, is related to the location where the boundary layer transitions from laminar to turbulent. The migration of the transition zone was linked to bead formation rate at the interface of the smooth and rough zones. Bead formation augments convective heat transfer, which will dry the downstream surface. As the downstream surface is dried, beads will begin to propagate upstream toward the stagnation point. The PICTUR video recordings confirmed the transition zone was established after the rough zone and contains smaller ice-roughness elements that grew closer to the stagnation point. Starting about halfway through the icing period, the PICTUR video shows evidence of light riming at times or possibly ice hydrometeors hitting and sticking to the icing surface. This occurs periodically only after the rough and transition zones were established. The contribution of ice particles to the total ice accretion is assumed to be negligible because the hydrometeor population is dominated by liquid droplets throughout the icing period.

IV. Numerical Simulation of Ice Accretion

Ice accretion on the PICTUR was modeled using the multishot approach with automatic remeshing in the numerical simulation package Ansys FENSAP-ICE [20,56]. Ice accretion is calculated in three consecutive steps: The flowfield solution is computed using the FENSAP flow solver module; the droplet impingement solution is computed using Eulerian particle tracking in the DROP3D module; and the water runback, ice accretion, and surface displacement calculations are computed using the ICE3D module. Automatic remeshing is completed using Ansys Fluent Meshing.

The flowfield around the PICTUR was simulated assuming steady-state, compressible, and viscous flow. The FENSAP solver is based on the Finite Element Method and models the flowfield using partial differential equations (PDEs) for the conservation of mass, momentum, and energy [56]. Turbulence is modeled using the single-equation Spalart–Allmaras (S-A) turbulence model, which considers the effect of surface roughness [57]. The particle transport system in DROP3D uses Eulerian formulation to solve the particle-flow problem as a continuum [56].

A. Numerical Methods

ICE3D calculates the surface displacement due to ice accretion for each node on the icing surface. The ice thickness h_{ice} is calculated normal to the iced surface and is defined as follows:

$$\Delta h_{\text{ice}} = \frac{\dot{m}_{\text{ice}}}{\rho_{\text{ice}}} \Delta t \tag{1}$$

where ρ_{ice} is the ice density, Δt is the time step length, and $\dot{m}_{\text{ice}}$ is the rate of ice accretion. The method by which $\dot{m}_{\text{ice}}$ is calculated depends on the type of icing being modeled. Rime ice is relatively simple to model numerically, where

$$\dot{m}_{\text{ice}} = \beta LWC_{\infty} V_{\infty} \tag{2}$$

where β is the droplet collection efficiency, which is the normalized value of the flux of liquid impingement on the icing surface, and LWC_{∞} and V_{∞} are the reference liquid water content and droplet velocity, respectively.

The glaze-ice model is characterized by a quasi-liquid film on the icing surface, which is subject to mass- and heat-transfer phenomena. The liquid film on the icing surface is produced by impinging droplets that do not freeze completely upon impact and may change shape (i.e., run back) due to acting forces. When modeling the mass-transfer phenomena of the film, ICE3D considers shear stresses generated by the airflow, centrifugal forces, and gravity. For heat-transfer phenomena, phase changes such as freezing, evaporation, and sublimation are considered. The glaze-ice model computes $\dot{m}_{\text{ice}}$ by solving a system of two PDEs closed by a set of conditions. The first PDE describes the conservation of mass:

$$\rho_f \left[\frac{\partial h_f}{\partial t} + \vec{\nabla} \cdot (\overline{V}_f h_f) \right] = \beta LWC_{\infty} V_{\infty} - \dot{m}_{\text{evap}} - \dot{m}_{\text{ice}} \tag{3}$$

where the subscript f identifies water film properties, meaning that h_f is the film thickness and $\overline{V}_f$ is the velocity of the water film averaged across the thickness and assuming zero velocity at the wall. The three terms on the right-hand side represent mass transfer by droplet impingement (source), liquid evaporation (sink), and ice accretion (sink). The second PDE used to model ice accretion is the energy conservation equation defined as

$$\begin{aligned} \rho_f \left[\frac{\partial h_f c_{p,f} T_f}{\partial t} + \vec{\nabla} \cdot (\overline{V}_f h_f c_{p,f} T_f) \right] &= \beta LWC_{\infty} V_{\infty} \left[e_d + \frac{V_d^2}{2} \right] \\ &- \dot{m}_{\text{evap}} L_{\text{evap}} + \dot{m}_{\text{ice}} (L_{\text{fusion}} - c_{p,\text{ice}} T_{\text{ice}}) + \sigma \varepsilon (T_{\infty}^4 - T_f^4) \\ &- c_h (T_f - T_{\text{rec}}) + q_{\text{anti-icing}} \end{aligned} \tag{4}$$

where c_p is the specific heat at a constant pressure for the film or ice, c_h is the convective heat- transfer coefficient, V_d is droplet velocity, T_{rec} is the recovery temperature, L_{evap} and L_{fusion} are the latent heats of evaporation and fusion, σ is the Boltzmann constant, ε is the emissivity, e_d is the droplet energy, and $q_{\text{anti-icing}}$ is the conductive heat flux. The terms on the right-hand side of Eq. (4) represent heat transfer generated by impinging droplets, evaporation, ice accretion, radiation, convection, and conduction (e.g., from an IPS), respectively. As described in Ref. [20], the evaporative heat flux term $\dot{m}_{\text{evap}} L_{\text{evap}}$ has significant influence on the ice growth when simulating glaze-ice conditions, rotating components such as helicopter rotors, and high-speed flows. The mass transfer due to evaporation $\dot{m}_{\text{evap}}$ is a function of vapor pressure, which is assumed to be uniform and equal to the ambient conditions when no vapor solution is available. The vapor solution provides a local estimate of vapor pressure and can be modeled throughout the domain using the vapor transport equation described in Ref. [58].

B. Simulation Domain and Boundary Conditions

The simulation domain is a rectangular volume (dimensions: 6.35-m high, 9.325-m long, and 2.54-m wide) that includes a half-model of the PICTUR placed at the domain wall due to symmetry. The model is centered about the domain's vertical axis and positioned three part-lengths from the inlet and five part-lengths from the outlet. The PICTUR icing surface is perpendicular to the inlet and level with the horizontal plane of the computational domain. The incident flowfield is defined by three velocity components u, v, w, which are calculated using the relative wind velocity from the perspective of the PICTUR. The surfaces of the PICTUR are defined as no-slip walls and the top, bottom, and side walls are defined as free-slip walls (see Table 2).

The volume of the domain is filled with an unstructured tetrahedral mesh and has a rectangular body of influence set up around the PICTUR geometry (see Supplementary Figs. S4 and S5; or go to the Supplemental Materials link that accompanies the electronic version of this article at http://arc.aiaa.org). The surface mesh along important icing surfaces and edges is refined to initially have a minimum element edge length of 2 mm. The boundary-layer effects are resolved using 30 layers of prismatic elements configured so that the maximum Y+ in the first layer is <1. In total, the original mesh contains about 12.9 million elements and 2.9 million nodes, which was found to be sufficient for simulating droplet collection efficiency and ice accretion on the leading edge of the cylinder. A mesh convergence analysis tested several refinement levels, including 50 prismatic layers, 16.4 million elements, and 3.6 million nodes. Meshes that were produced during the automatic remeshing process use Ansys Fluent. Settings in Ansys Fluent were configured to produce surface and volume meshes that had refinement levels equal to or greater than that of the original mesh. Simulations with complex ice growth can result in the final mesh becoming double the size of the original mesh.

C. General Simulation Configuration

The simulation input parameters used in this study are computed using the data presented in Fig. 2. Input parameters are either averaged over the full icing period to produce a single set of values or averaged over the duration of each shot to produce multiple sets of values (one for each shot). Input parameters are not averaged with any weighting scheme, and data-filtering methods are not used unless explicitly stated. All simulation settings were configured to align with the recommendations found in the literature. The small-scale ice surface roughness, which affects the heat transfer at the icing surface, was calculated using the analytical beading model developed for Ansys FENSAP-ICE [59,60]. This model is embedded in the ice accretion solver and predicts the small-scale sand-grain roughness that results from liquid beads on the icing surface. These liquid beads do not freeze nor add any visible texture to the final ice shape in the simulation. The roughness estimation is an output of the icing solver and an input of the flow solver, and therefore can only be used in the following shot in a multishot simulation. This means small-scale surface roughness was not considered in any single-shot simulations nor in the first shot of any multishot simulations. In these cases, no roughness was assumed.

Ice density is an important characteristic of ice accretion. In most icing simulations, ice density is a user-defined input parameter commonly set to a value of 917 $\text{kg} \times \text{m}^{-3}$. The so-called variable-impact ice-density model is a beta feature in Ansys FENSAP-ICE Ver. 2023, which computes ice density using an analytical model. This beta feature was introduced in simulations pertaining to the 2nd AIAA Ice Prediction Workshop [61] and was shown to produce realistic ice shapes that were comparable to wind-tunnel experiments. The variable-impact ice-density model was activated for this study.

Table 2 Summary of simulation domain settings

Location	Boundary condition
PICTUR surface	No-slip wall
PICTUR midplane	Symmetry
Top, bottom, side walls	Free-slip wall
Front wall	Inlet (vel. components, temp., pres.)
Rear wall	Outlet (pres.)

The splashing and bouncing effects of SLD were modeled using the postprocessing option in Ansys FENSAP-ICE coupled with the Mundo model [62,63], and the acceleration due to gravity ($9.8\ \text{m} \times \text{s}^{-2}$) was also considered. Several different combinations of modeling options for SLD were tested, including, e.g., replacing the Mundo model with other models such as the Honsek model [64] and activating droplet reinjection. These alternative combinations of modeling options produced inconsequential changes to the collection efficiency curves and the final ice shape when compared to the settings that were used.

The cumulative mass vs diameter curve shown in Supplementary Fig. S3 (or go to the Supplemental Materials link that accompanies the electronic version of this article at http://arc.aiaa.org) indicates that, on average, nearly all (~99.7%) of the liquid water content was contained within droplets that have diameters <300 μm. The collection efficiency curves for several different droplet diameters between 6 and 300 μm were simulated using the bare PICTUR cylinder. The collection efficiency curves shown in Fig. 4 reveal that efficiency increases with droplet diameter from 6 to ~50 μm, after which it remains virtually unchanged for droplets up to 300 μm. This means that droplets ranging between 50 and 300 μm (a population that represents ~35% of the total LWC) are practically unaffected by the flowfield around the cylinder, as their sizable mass and freestream momentum cause them to deviate from the flow's path, penetrate through the high-pressure region produced by the cylinder, and impact its surface. Put in the context of numerical simulations, using a single-diameter model based on an MVD of 50 μm or higher will lead to a higher collection efficiency when compared to a multidiameter model that includes droplets less than 50 μm. This is because the multidiameter model combines the collection efficiencies of all diameters into a singular effective collection-efficiency curve using a weighted average scheme that is based upon their relative contribution to the total liquid water content [56]. This study simulates ice accretion using the period- or shot-averaged MVD value, which is typically greater than or equal to 50 μm (leading to an overall conservative estimate of collection efficiency and ice accretion).

D. Comparing Multishot Techniques

The LWC and static air temperature were identified as user-defined input parameters that have significant impact on ice accretion. The LWC (and temperature to a lesser extent) is dynamic throughout the icing period, which is a feature of natural icing conditions that adds to the complexity of simulating a steady-state wind-tunnel experiment. Beyond the fact that more shots increase the resolution of ice features, the multishot technique does not have an established "best practice" for selecting the ideal number and length of shots. When this technique is used in literature, shots are seemingly always initiated using the same input parameters and shot lengths, which is acceptable for simulating steady-state conditions. However, it is not clear whether this dynamic icing period should be simulated using period- or shot-averaged input parameters.

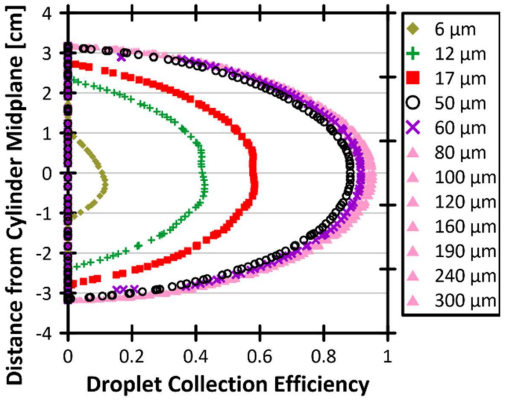

Fig. 4 Collection efficiency of several droplet diameters on the leading-edge surface of the PICTUR cylinder.

In order to determine whether the dynamic icing period presented in Fig. 2 could benefit from being simulated using shot-averaged input parameters, three simulations were performed: 1) one-shot simulation that uses a single set of icing parameters averaged over the entire icing period; 2) seven-shot simulation that uses for every shot the same single set of icing parameters used in Sim 1; and 3) seven-shot simulation that uses seven sets of shot-averaged icing parameters. Because the experimental data indicated the icing intensity was greatest within the first 150 s of accretion, it was deemed important to discretize the beginning of the icing period with a higher resolution to promote the early formation of sizable roughness elements. Extending shot length near the end of the simulation was expected to simply grow any features that had been already established. Thus, both multishot simulations use a $30 \times 5/200/240$-s shot breakdown (summing to 590 s) to allow for a direct comparison of results. Heat fluxes were calculated using the classical technique, where all icing surfaces are set as isothermal with a wall temperature ~10°C above the expected adiabatic stagnation temperature of the flow. The recovery factor, which is used to better predict the energy lost at the icing surface due to friction effects, was set to 0.9 throughout this study [65]. For context, a recovery factor equal to unity means the surface temperature is equal to the freestream stagnation temperature. The input parameters used for these icing simulations are shown in Table 3.

The final ice shape for each simulation, including cross-section profiles at one-third of the span length from the cylinder tip, are presented in Fig. 5. In general, these simulations appear to predict the overall shape of ice accretion well. The thickest point of ice accretion for Sim 1 occurred at a 90-deg rotation from the stagnation point. This ridge formed so far aft of the other simulations, whose thickest-point ice accretion occurred near the 45-deg mark, likely because the single-shot simulation did not consider surface roughness (recall the surface roughness model is only effective in multishot simulations). In the multishot simulations, the small-scale surface roughness (predicted by the software to have bead heights in the submillimeter range) increased the magnitude of heat transfer at the icing surface, causing liquid to freeze closer to the stagnation point, and before it could run all the way back to the cylinder edges. Due to the constant icing conditions in Sim 2, accretion tended to occur at the same location for each shot, which formed one thick ridge of ice. The varying conditions in Sim 3 caused three thinner ridges to form in different downstream locations, which are within the experimental range of the rough and transition zones. The aftmost ridge was formed by the end of Shot 5 and the two upstream ridges were grown during Shots 6 and 7. The low LWC in Shots 6 and 7 formed relatively thin liquid films that, due to their reduced mass and thermal capacity, had less severe runback and froze upstream of the existing accretion boundaries of the preceding shot. This suggests the reduction in LWC during the flight test likely helped to grow the transition zone toward the stagnation point. Although these simulations do not produce sizable roughness elements comparable to the experimental results, they illustrate how multiple sets of input parameters can be used to capture changes in icing intensity that influence where ice features are formed.

In addition to the location of ice features, the shot-averaged input parameters can influence the total liquid catch and ice growth (by mass). Although the PICTUR was exposed to varying levels of LWC throughout Sim 3, the total amount of LWC exposure, i.e., the sum of LWC × time, was within 2% of the other simulations (this difference is attributed to shot-average rounding errors). The catch profiles inferred from the geometric extents of the ice cross sections in Fig. 5 suggest that Sim 1 should have caught the most liquid. However, because this was a single-shot simulation, liquid impingement was only computed for the bare cylinder. Simulation 2 has the largest liquid catch in Fig. 6 because this multishot simulation considered the periodic growth of its catch profile due to ice accretion, which grew to be broader than the other multishot simulation. The total liquid catch is lowest for Sim 3 because its icing profile tended to grow into the oncoming flow rather than become perpendicular to it, producing small shadow zones aft of its ridges, which reduced its overall collection efficiency.

Table 3 The period- and shot-averaged input parameters used in simulations to compare the different techniques

Sim	Shot	Duration, s	Static pres., Pa	Static temp., °C	LWC, g m^{-3}	MVD, μm	Long. Vel., m s^{-1}	Lat. Vel., m s^{-1}	Vert. Vel., m s^{-1}
1	1	590	66320	−3.2	0.11	67	92	6	5
2	1—7	30 × 5/200/240	66320	−3.2	0.11	67	92	6	5
3	1	30	66338	−3.6	0.25	50	94	5	4
	2	30	66276	−3.7	0.32	50	91	6	5
	3	30	66429	−3.8	0.31	58	91	6	5
	4	30	66357	−3.6	0.27	50	88	6	5
	5	30	66351	−3.3	0.18	21	89	6	5
	6	200	66335	−3.2	0.07	74	93	5	5
	7	240	66290	−3	0.04	75	92	5	5

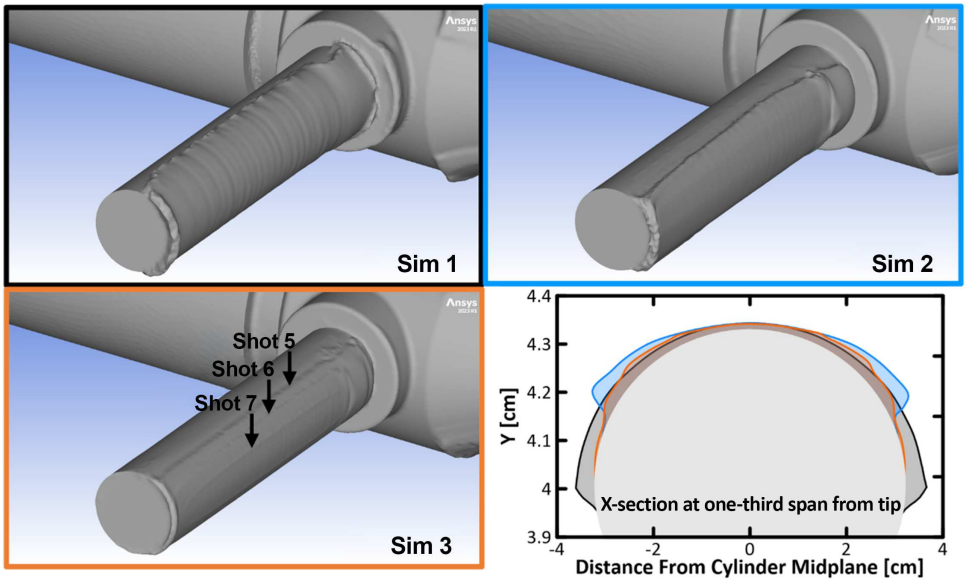

Fig. 5 Final ice shapes and a cross-sectional view of the ice profile at one-third span from the tip of the PICTUR cylinder for Sims 1–3.

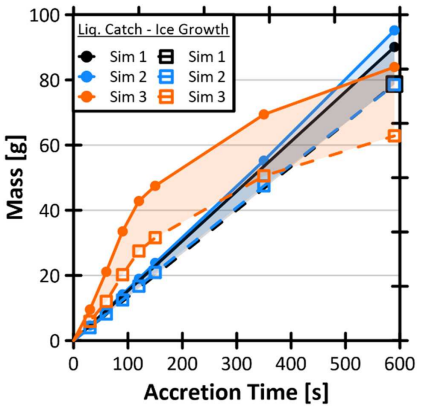

Fig. 6 The liquid catch and ice growth vs time for Sims 1–3.

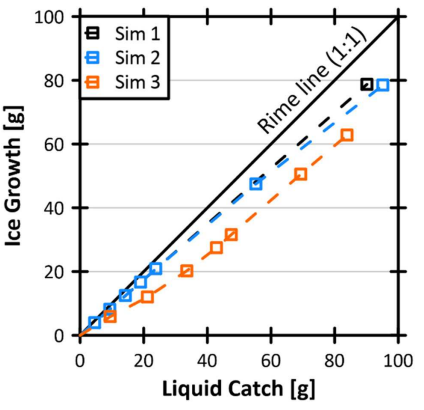

Fig. 7 The ratio of ice growth vs liquid catch for Sims 1–3.

The high LWC shots at the beginning of Sim 3 exposed the PICTUR to more than twice as much liquid by the end of Shot 5 (150 s) when compared to the other simulations in Fig. 7. Due to this increased exposure, Sim 3 accreted 51% more ice than the other simulations by the 150-s mark. Although ice-accretion levels were elevated during this time, the freezing fraction of Sim 3 was relatively poor, resulting in 25% less ice accretion when compared to the other simulations at the 50-g liquid catch level in Fig. 7. The freezing fraction in Sim 3 recovers slightly during the last two shots but the total amount of ice accretion by the end of the icing period is still at 80% of the other simulations. Based on these results, high LWC shots in shot-averaged simulations reduce freezing fraction levels, which can lead to a reduction in total ice accretion.

E. Comparing Heat Flux Techniques

The extended ice data (EID) calculation with vapor solution (EID + Vapor Solution) is an alternative to the classical technique for calculating heat fluxes at the icing surface and requires setting all icing surfaces to be adiabatic [56]. The EID calculation and vapor solution must be used together in Ver. 2023 of this software. The EID calculation is a proprietary Ansys FENSAP-ICE technology that extracts heat-transfer coefficients from adiabatic flow regimes. The EID calculation is useful for glaze-icing conditions when the wall temperature cannot be easily related to the stagnation temperature through a recovery factor. Preliminary testing suggested that the distribution of evaporative heat flux at the icing surface is affected by the technique used to compute heat flux. Small changes to the

evaporative heat flux in a single-shot simulation may be inconsequential, but propagating this change through a multishot simulation may influence the total accretion and final ice shape. To investigate this further, Sim 3, which was originally run using the classical technique, was rerun using the EID + Vapor Solution technique. Results from these two simulations are shown in Fig. 8, which includes the cross-section ice profile for each shot and the evaporative heat flux distribution for Shots 1 and 7 (at one-third span distance from the cylinder tip).

The two techniques produce similar evaporative heat flux distributions in Shot 1, however, the EID + Vapor Solution has slightly elevated flux levels closer to the cylinder's edges and reduced levels near the stagnation point. By Shot 5, the elevated flux levels caused the EID + Vapor Solution to grow a ridge that is thicker and positioned farther aft of the classical solution. This resulted in a broadened ice profile that led to slightly elevated levels of liquid catch (+5%) and ice accretion (+8%) by the end of the icing period. Both simulations grew three distinct ridges of accretion, which are clustered more closely together in the EID + Vapor Solution, producing a surface unevenness that better resembles the rough zone in the experimental results. Ridge positioning aligns with the features of the evaporative heat flux distributions in Shot 7. The location of maximum flux is positioned farther downstream in the EID + Vapor Solution, and the extent of the icing surface that is exposed to relatively high levels of evaporative heat flux (e.g., shaded region $\gtrsim$1200) is also greater. Increasing the amount of surface area that is exposed to elevated flux levels in turn increases the potential to form ice features, which is the main benefit of the EID + Vapor Solution.

F. Combining Techniques, Increasing Shots, and Applying LWC Filter

Ansys FENSAP-ICE is capable of modeling complex ice features such as scallops, lobster tails, and detailed glaze-horns in a variety of steady-state icing conditions, including, for instance, when the LWC is near 0.3 g × m^{-3}, the icing period is 9- min long, the number of shots is <10, or the shot duration is >40 s. However, when these properties are combined in a single simulation as they are in this study (i.e., low average LWC level of 0.11 g × m^{-3}; high static air temperature of −3.3°C; and a short icing period, which includes 3 min of high-intensity icing followed by 6 min of low-intensity icing), the software seemingly struggles to generate sizable roughness elements with the same level of detail observed during flight. Because the period-averaged multishot technique and the EID + Vapor Solution technique formed the broadest ice shapes with relatively high levels of liquid catch and total accretion, these settings were selected for a simulation with an elevated number of shots (12). A more potent icing environment was generated for this simulation by filtering the icing period to remove intervals where LWC <0.01 g × m^{-3}, which would bias the average LWC toward a lower value. This shortened the icing period to 463 s and raised the average LWC from 0.11 to 0.14 g × m^{-3}. The period-averaged input parameters produced from the shortened icing period are shown in Table 4 and the final shape of accretion is presented in Fig. 9.

Considering the reduced duration and elevated LWC, this simulation still accreted 74 g of ice, which is within 6% of Sims 1 and 2. The final ice shape in Fig. 9 shows how this simulation grew two ridges, one on top of the other, using a single period-averaged set of input parameters. The aftmost ridge was formed first, and its presence augmented the upstream flowfield and heat transfer enough to grow the foremost ridge closer to the stagnation point. The process by which the foremost ridge was formed resembles the way the transition zone grew toward the stagnation point during the flight test. The foremost

Table 4 The period-averaged set of input parameters used in the combined simulation

Property	Value
Shots	12
Duration, s	Shot 1: 23 s Shots 2–12: 40 s
Static pres., Pa	66,332
Static temp., °C	−3.3
LWC, g × m^{-3}	0.14
MVD, μm	54
Long. Vel., m × s^{-1}	92
Lat. Vel., m × s^{-1}	6
Vert. Vel., m × s^{-1}	5

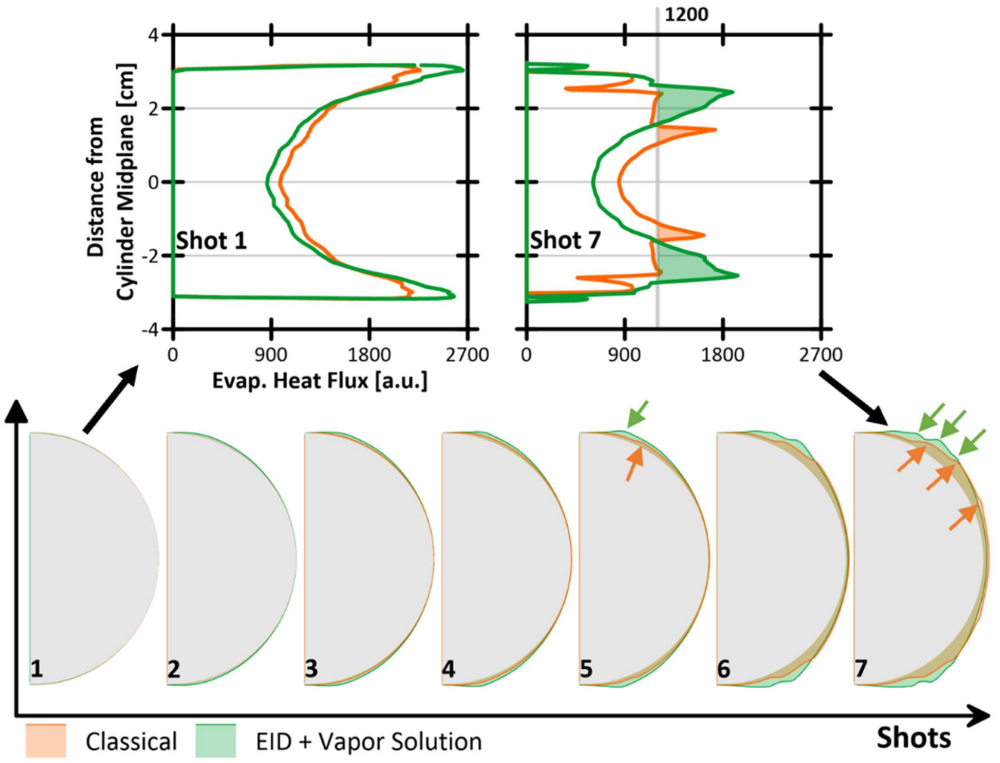

Fig. 8 Cross-sectional view of the ice profile for each shot and the evaporative heat flux distribution for Shots 1 and 7 at one-third span from the tip of the PICTUR cylinder.

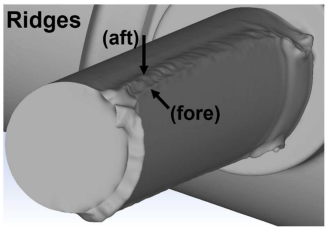

Fig. 9 Close-up view of the trailing-edge ice accretion produced by the combined simulation.

ridge protrudes about 1 mm above the icing surface, and if more ridges could be formed in this manner by using more shots, the unevenness of the icing surface would resemble the experimental results more closely. The simulation-estimated bead height, which is important for calculating accurate aerodynamic properties in addition to heat fluxes, is estimated to be around 0.7 mm at maximum near the rough zone. This suggests that the addition of millimeter-scale (or larger) physical roughness elements to the ice surface will not only match the look of the flight-test ice shape more closely but could further increase the amount of drag caused by ice accretion as determined through numerical simulation. In cases where the simulation is unable to grow sizable roughness elements or estimate the sand-grain roughness height naturally, the height and distribution of sand-grain roughness can be defined by the user to best resemble the experimental ice shape prior to performing drag simulations (e.g., setting the sand-grain height to the relatively large value of 3 or 4 mm in the expected rough zone and smaller heights in the transition and smooth zones).

V. Conclusions

A 590-s-long glaze-icing period in Appendix O conditions was selected from the 2022 Winter Precipitation Type Research Multi-Scale Experiment (WINTRE-MIX) campaign data for simulation using a commercially available numerical ice-accretion software package. All simulation input parameters were measured directly or were calculated using flight-test data. Simulation results were qualitatively compared to a high-resolution video of ice accretion on the cylindrical test article of the Platform for Ice-accretion and Coatings Tests with Ultrasonic Readings (PICTUR), which was mounted on a pylon under the aircraft wing. The multishot with an automatic remeshing approach within Ansys FENSAP-ICE was used to simulate ice accretion on the PICTUR. The conditions during this icing period were dynamic, unlike the typical steady-state wind-tunnel experiments. A seven-shot simulation using shot-averaged input parameters was compared to the standard multishot method, which uses a single set of input parameters averaged over the entire icing period. The standard multishot method produced a broader ice profile, had a larger liquid catch, and accreted more ice (a 20% increase by mass) than the shot-averaged simulation. The two methods available in Ansys FENSAP-ICE Ver. 2023 for calculating heat fluxes at the icing surface were also compared, namely the classical technique and the extended icing data with the vapor-solution technique. The extended icing data with vapor solution elevated the evaporative heat flux levels in the area where glaze-ice features typically form, which generated a broader ice profile with slightly elevated liquid catch (+5%) and total accretion (+8%) in comparison to the classical technique. A simulation combining the standard multishot technique and the extended icing data with the vapor-solution technique was performed with an increased number of shots (12), using data that was filtered to remove intervals of low-liquid-water content. This simulation captured the general shape of the ice and proved capable of growing sizable surface elements similar to how they were observed to grow experimentally. That said, no combination of simulation settings, input parameters, and multishot methods tested in this study generated the same level of surface detail observed in the experiment. Capturing surface details such as sizable surface-roughness elements is important for determining accurate aerodynamic penalties of ice accretion and is necessary for identifying aircraft and ice protection system (IPS) performance limitations in icing conditions using numerical techniques.

Acknowledgments

The authors would like to acknowledge the National Research Council of Canada (NRC) Aeronautical Product Development and Certification (APDC) program for funding this research, the NRC New Beginnings Ideation program for funding the development of the Platform for Ice-accretion and Coatings Tests with Ultrasonic Readings (PICTUR), the USA National Science Foundation (NSF) Division of Atmospheric and Geospace Sciences (AGS) Grant No. 2113995 for funding the data collection through research flights. The authors thank Stratton Park Engineering Company incorporated (SPEC) Inc. for the loan of the high-volume precipitation spectrometer Ver. 3 (HVPS-3) probe. The authors acknowledge Dan Fuleki and Nicholas Doiron for their provision of processed ultrasonic ice-accretion sensor (UIAS) data and previous Carleton University researchers Kaniz Ronak Sultana and Ayesh Sudasinghe, who worked on the early stages of this project and established the foundations of this study. The authors acknowledge both Justin Minder, the lead Principal Investigator (PI) of the Winter Precipitation Type Research Multi-Scale Experiment (WINTRE-MIX) campaign, and Mengistu Wolde, the facility manager for the NRC Convair-580, for enabling the data collection. The authors also acknowledge the co-PIs of the WINTRE-MIX campaign, weather forecasters, flight crew, and instrumentation and maintenance teams that made the WINTRE-MIX campaign successful.

References

[1] Transportation Safety Board of Canada, "In-Flight Icing and Collision with Terrain: Mooney M20K, C-GQMS," A22W0027, Gatineau, QC, Oct. 2022.

[2] Cao, Y., Tan, W., and Wu, Z., "Aircraft Icing: An Ongoing Threat to Aviation Safety," *Aerospace Science and Technology*, Vol. 75, April 2018, pp. 353–385. https://doi.org/10.1016/j.ast.2017.12.028

[3] Gent, R. W., Dart, N. P., and Cansdale, J. T., "Aircraft Icing," *Philosophical Transactions of the Royal Society A: Mathematical, Physical and Engineering Sciences*, Vol. 358, No. 1776, 2000, pp. 2873–2911. https://doi.org/10.1098/rsta.2000.0689

[4] National Transportation Safety Board, "In-Flight Icing Encounter and Loss of Control: Simmons Airlines, American Eagle Flight 4184," NTSB/AAR-96/01, Washington, D.C., June 1996.

[5] Bernstein, B., DiVito, S., Riley, J. T., Landolt, S., Haggerty, J., Thompson, G., Adriaansen, D., Serke, D., Kessinger, C., Tessendorf, S., et al., "The In-Cloud Icing and Large-Drop Experiment (ICICLE) Science and Operations Plans," DOT/FAA/TC-21/29, Atlantic City, NJ, 2021.

[6] Petty, K. R., and Floyd, D. J., "A Statistical Review of Aviation Airframe Icing Accidents in the U.S," *Proceedings of the 11th AMS Conference on Aviation, Range, and Aerospace*, American Meteorology Soc., 2004, pp. 623–628.

[7] Bragg, M. B., Broeren, A. P., and Blumenthal, L. A., "Iced-Airfoil Aerodynamics," *Progress in Aerospace Sciences*, Vol. 41, No. 5, 2005, pp. 323–362. https://doi.org/10.1016/J.PAEROSCI.2005.07.001

[8] Federal Aviation Administration, "Pilot Guide: Flight in Icing Conditions," AC 91-74B, Oct. 2015.

[9] Lynch, F. T., and Khodadoust, A., "Effects of Ice Accretions on Aircraft Aerodynamics," *Progress in Aerospace Sciences*, Vol. 37, No. 8, 2001, pp. 669–767. https://doi.org/10.1016/S0376-0421(01)00018-5

[10] Mauery, T., Alonso, J., Cary, A., Lee, V., Mavriplis, D., Medic Pratt, G., Hartford, E., John Schaefer, C., and Slotnick, J., "A Guide for Aircraft Certification by Analysis," NASA CR-20210015404, May 2021.

[11] Taszarek, M., Kendzierski, S., and Pilguj, N., "Hazardous Weather Affecting European Airports: Climatological Estimates of Situations with Limited Visibility, Thunderstorm, Low-Level Wind Shear and Snowfall from ERA5," *Weather and Climate Extremes*, Vol. 28, June 2020, Paper 100243. https://doi.org/10.1016/j.wace.2020.100243

[12] Intergovernmental Panel on Climate Change, *Climate Change 2007: The Physical Science Basis. Contribution of Working Group 1 to the Fourth Assessment Report of the Intergovernmental Panel on Climate Change*, Cambridge Univ. Press, Cambridge, England, U.K. and New York, 2007.

[13] Federal Aviation Administration, "U.S. Code of Federal Regulations: Appendix C to Part 25, Title 14 - Atmospheric Icing Conditions," 1999.

[14] Federal Aviation Administration, "U.S. Code of Federal Regulations: Appendix O to Parts 25 and 33, Title 14 - Airplane and Engine Certification Requirements in Supercooled Large Drop, Mixed Phase, and Ice Crystal Conditions," 2015.

[15] Brahimi, M. T., Tran, P., Chocron, D., Tezok, F., and Paraschivoiu, I., "Effects of Supercooled Large Droplets on Ice Accretion Characteristics," *35th Aerospace Sciences Meeting and Exhibit*, AIAA Paper 1997-0306, 1997.
https://doi.org/10.2514/6.1997-306

[16] Yamazaki, M., Jemcov, A., and Sakaue, H., "A Review on the Current Status of Icing Physics and Mitigation in Aviation," *Aerospace*, Vol. 8, No. 7, 2021, p. 188.
https://doi.org/10.3390/aerospace8070188

[17] Habashi, W., "Recent Advances in CFD for In-Flight Icing Simulation," *Journal of Japan Society of Fluid Mechanics*, Vol. 28, No. 2, 2009, pp. 98–118.

[18] Beaugendre, H., Morency, F., and Habashi, W. G., "FENSAP-ICE's Three-Dimensional In-Flight Ice Accretion Module: ICE3D," *Journal of Aircraft*, Vol. 40, No. 2, 2003, pp. 239–247.
https://doi.org/10.2514/2.3113

[19] Morency, F., Beaugendre, H., Baruzzi, G., and Habashi, W. G., "FENSAP-ICE: A Comprehensive 3D Simulation System for In-Flight Icing," *15th AIAA Computational Fluid Dynamics Conference*, AIAA Paper 2001-2566, June 2001.

[20] Ozcer, I., Switchenko, D., Baruzzi, G. S., and Chen, J., "Multi-Shot Icing Simulations with Automatic Re-Meshing," SAE Technical Paper 2019-01-1956, 2019.
https://doi.org/10.4271/2019-01-1956

[21] Bidwell, C. S., and Potapczuk, M. G., *Users Manual for the NASA Lewis Three-Dimensional Ice Accretion Code (LEWICE 3D)*, NASA, Cleveland, OH, Dec. 1993.

[22] Szilder, K., and Lozowski, E., "Initial Verification of a 3D Morphogenetic Model of In-Flight Icing on a Cylinder," *Proceedings of the 24th Congress of the International Council of the Aeronautical Sciences*, 2004, Paper ICAS 2004-P.19.

[23] Radenac, E., Gaible, H., Bezard, H., and Reulet, P., "IGLOO3D Computations of the Ice Accretion on Swept-Wings of the SUNSET2 Database," SAE Technical Paper 2019-01-1935, 2019.
https://doi.org/10.4271/2019-01-1935

[24] Radenac, E., and Duchayne, Q., "IGLOO3D Simulations of the 1st AIAA Ice-Prediction-Workshop Database," *2022 AIAA Aviation Forum*, AIAA Paper 2022-3310, 2022.
https://doi.org/10.2514/6.2022-3310

[25] Gori, G., Zocca, M., Garabelli, M., Guardone, A., and Quaranta, G., "PoliMIce: A Simulation Framework for Three-Dimensional Ice Accretion," *Applied Mathematics and Computation*, Vol. 267, Sept. 2015, pp. 96–107.
https://doi.org/10.1016/j.amc.2015.05.081

[26] Morelli, M., Bellosta, T., Donizetti, A., and Guardone, A., "Assessment of the PoliMIce Toolkit from the 1st AIAA Ice Prediction Workshop," *2022 AIAA Aviation Forum*, AIAA Paper 2022-3307, 2022.
https://doi.org/10.2514/6.2022-3307

[27] Cinquegrana, D., D'Aniello, F., de Rosa, D., Carozza, A., Catalano, P., and Mingione, G., "A CIRA 3D Ice Accretion Code for Multiple Cloud Conditions Simulations," SAE Technical Paper 2023-01-1461, 2023.
https://doi.org/10.4271/2023-01-1461

[28] Hedde, T., and Guffond, D., "ONERA Three-Dimensional Icing Model," *AIAA Journal*, Vol. 33, No. 6, 1995, pp. 1038–1045.
https://doi.org/10.2514/3.12795

[29] Villedieu, P., Trontin, P., Guffond, D., and Bobo, D., "SLD Lagrangian Modeling and Capability Assessment in the Frame of ONERA 3D Icing Suite," *4th AIAA Atmospheric and Space Environments Conference*, AIAA Paper 2012-3132, 2012.
https://doi.org/10.2514/6.2012-3132

[30] Laurendeau, E., Bourgault-Cote, S., Ozcer, I. A., Hann, R., Radenac, E., and Pueyo, A., "Summary from the 1st AIAA Ice Prediction Workshop," *2022 AIAA Aviation Forum*, AIAA Paper 2022-3398, 2022.
https://doi.org/10.2514/6.2022-3398

[31] Reehorst, A. L., "Prediction of Ice Accretion on a Swept NACA 0012 Airfoil and Comparisons to Flight Test Results," *30th AIAA Aerospace Sciences Meeting and Exhibit*, AIAA Paper 1992-0043, 1992.

[32] Vargas, M., Giriunas, J. A., and Ratvasky, T. P., "Ice Accretion Formations on a NACA 0012 Swept Wing Tip in Natural Icing Conditions," *40th AIAA Aerospace Sciences Meeting and Exhibit*, AIAA Paper 2002-0244, 2002.
https://doi.org/10.2514/6.2002-244

[33] Nichman, L., Fuleki, D., Song, N., Benmeddour, A., Wolde, M., Orchard, D., Matida, E., Bala, K., Sun, Z., Bliankinshtein, N., et al., "Airborne Platform for Ice-Accretion and Coatings Tests with Ultrasonic Readings (PICTUR)," SAE Technical Paper 2023-01-1431, 2023.
https://doi.org/10.4271/2023-01-1431

[34] Hansman, R. J., Yamaguchi, K., Berkowitz, B., and Potapczuk, M., "Modeling of Surface Roughness Effects on Glaze Ice Accretion," *Journal of Thermophysics and Heat Transfer*, Vol. 5, No. 1, 1991, pp. 54–60.
https://doi.org/10.2514/3.226

[35] Baumert, A., Bansmer, S., Trontin, P., and Villedieu, P., "Experimental and Numerical Investigations on Aircraft Icing at Mixed Phase Conditions," *International Journal of Heat and Mass Transfer*, Vol. 123, Aug. 2018, pp. 957–978.
https://doi.org/10.1016/j.ijheatmasstransfer.2018.02.008

[36] Minder, J. R., Bassill, N., Fabry, F., French, J. R., Friedrich, K., Gultepe, I., Gyakum, J., Kingsmill, D. E., Kosiba, K., Lachapelle, M., et al., "P-Type Processes and Predictability: The Winter Precipitation Type Research Multiscale Experiment (WINTRE-MIX)," *Bulletin of the American Meteorological Society*, Vol. 104, No. 8, 2023, pp. E1469–E1492.
https://doi.org/10.1175/BAMS-D-22-0095.1

[37] Fuleki, D., Sun, Z., Wu, J., Lothrop, A., and Gee, A., "Implementation of a Non-Intrusive Ultrasound Ice Accretion Sensor to an ALF502R-5 Vane Segment Ice Crystal Component Test," *2022 AIAA Aviation Forum*, AIAA Paper 2022-3697, 2022.
https://doi.org/10.2514/6.2022-3697

[38] Nguyen, C. M., Wolde, M., Battaglia, A., Nichman, L., Bliankinshtein, N., Haimov, S., Bala, K., and Schuettemeyer, D., "Coincident in Situ and Triple-Frequency Radar Airborne Observations in the Arctic," *Atmospheric Measurement Techniques*, Vol. 15, No. 3, 2022, pp. 775–795.
https://doi.org/10.5194/amt-15-775-2022

[39] Shakirova, A., Nichman, L., Belacel, N., Nguyen, C., Bliankinshtein, N., Wolde, M., DiVito, S., Bernstein, B., and Huang, Y., "Multivariable Characterization of Atmospheric Environment with Data Collected in Flight," *Atmosphere*, Vol. 13, No. 10, 2022, p. 1715.
https://doi.org/10.3390/ATMOS13101715

[40] Bala, K., and Wolde, M., "WINTRE-MIX: NRC Convair 580 Atmospheric and Aircraft State Data V1.0," UCAR/NCAR—Earth Observing Lab., 2022.
https://doi.org/10.26023/BHS6-TEVC-GR04

[41] Korolev, A. V., Strapp, J. W., Isaac, G. A., and Nevzorov, A. N., "The Nevzorov Airborne Hot-Wire LWC–TWC Probe: Principle of Operation and Performance Characteristics," *Journal of Atmospheric and Oceanic Technology*, Vol. 15, No. 6, 1998, pp. 1495–1510.
https://doi.org/10.1175/1520-0426(1998)015<1495:TNAHWL>2.0.CO;2

[42] Korolev, A., Strapp, J. W., Isaac, G. A., and Emery, E., "Improved Airborne Hot-Wire Measurements of Ice Water Content in Clouds," *Journal of Atmospheric and Oceanic Technology*, Vol. 30, No. 9, 2013, pp. 2121–2131.
https://doi.org/10.1175/JTECH-D-13-00007.1

[43] Schwarzenboeck, A., Mioche, G., Armetta, A., Herber, A., and Gayet, J.-F., "Response of the Nevzorov Hot Wire Probe in Clouds Dominated by Droplet Conditions in the Drizzle Size Range," *Atmospheric Measurement Techniques*, Vol. 2, No. 2, 2009, pp. 779–788.
https://doi.org/10.5194/amt-2-779-2009

[44] Faber, S., French, J. R., and Jackson, R., "Laboratory and In-Flight Evaluation of Measurement Uncertainties from a Commercial Cloud Droplet Probe (CDP)," *Atmospheric Measurement Techniques*, Vol. 11, No. 6, 2018, pp. 3645–3659.
https://doi.org/10.5194/amt-11-3645-2018

[45] Abel, S. J., Cotton, R. J., Barrett, P. A., and Vance, A. K., "A Comparison of Ice Water Content Measurement Techniques on the FAAM Bae-146 Aircraft," *Atmospheric Measurement Techniques*, Vol. 7, No. 9, 2014, pp. 3007–3022.
https://doi.org/10.5194/amt-7-3007-2014

[46] Lawson, P., Gurganus, C., Woods, S., and Bruintjes, R., "Aircraft Observations of Cumulus Microphysics Ranging from the Tropics to Midlatitudes: Implications for a 'New' Secondary Ice Process," *Journal of the Atmospheric Sciences*, Vol. 74, No. 9, 2017, pp. 2899–2920.
https://doi.org/10.1175/JAS-D-17-0033.1

[47] Lawson, R. P., O'Connor, D., Zmarzly, P., Weaver, K., Baker, B., Mo, Q., and Jonsson, H., "The 2D-S (Stereo) Probe: Design and Preliminary Tests of a New Airborne, High-Speed, High-Resolution Particle Imaging Probe," *Journal of Atmospheric and Oceanic Technology*, Vol. 23, No. 11, 2006, pp. 1462–1477.
https://doi.org/10.1175/JTECH1927.1

[48] SPEC Inc, "HVPS V3 Technical Manual: A High Volume Precipitation Spectrometer (Rev 1.2)," Boulder, CO, 2013.

[49] Praz, C., Ding, S., McFarquhar, G. M., and Berne, A., "A Versatile Method for Ice Particle Habit Classification Using Airborne Imaging

Probe Data," *Journal of Geophysical Research: Atmospheres*, Vol. 123, No. 23, 2018, pp. 13,472–13,495.
https://doi.org/10.1029/2018JD029163

[50] Baumgardner, D., Abel, S. J., Axisa, D., Cotton, R., Crosier, J., Field, P., Gurganus, C., Heymsfield, A., Korolev, A., Krämer, M., et al., "Cloud Ice Properties: In Situ Measurement Challenges," *Meteorological Monographs*, Vol. 58, Jan. 2017, pp. 9.1–9.23.
https://doi.org/10.1175/AMSMONOGRAPHS-D-16-0011.1

[51] Bliankinshtein, N., "WINTRE-MIX: NRC Convair 580 Cloud Bulk Microphysics Data V1.0," UCAR/NCAR—Earth Observing Lab., 2022.
https://doi.org/10.26023/7FFB-FR7C-010C

[52] Nichman, L., Wolde, M., Ranjbar, K., and Bala, K., "WINTRE-MIX: NRC Convair 580 Scattering and Optical Array Probe Microphysics Data V1.0," UCAR/NCAR—Earth Observing Lab., 2022.
https://doi.org/10.26023/XNM4-MJP0-4Q0H

[53] Milani, Z., "10-Minute Video of Ice Accretion on the PICTUR Cylinder During WINTRE-MIX Flight 06 V1.0," Borealis, 2023.
https://doi.org/10.5683/SP3/CQHHM4

[54] Jackson, D., Anderson, K., and Heuer, W., "Liquid Water Detection Algorithm for the Magnetostrictive Ice Detector," SAE Technical Paper 2023-01-1430, 2023.
https://doi.org/10.4271/2023-01-1430

[55] Hansman, R. J., and Turnock, S. R., "Investigation of Surface Water Behavior During Glaze Ice Accretion," *Journal of Aircraft*, Vol. 26, No. 2, 1989, pp. 140–147.
https://doi.org/10.2514/3.45735

[56] *Ansys FENSAP-ICE User Manual*, Release 2022 R2, Ansys, Canonsburg, PA, July 2022.

[57] Aupoix, B., and Spalart, P. R., "Extensions of the Spalart—Allmaras Turbulence Model to Account for Wall Roughness," *International Journal of Heat and Fluid Flow*, Vol. 24, No. 4, 2003, pp. 454–462.
https://doi.org/10.1016/S0142-727X(03)00043-2

[58] Zhang, Y., Ozcer, I., Nilamdeen, S., Baruzzi, G. S., and Selvanayagam, J., "Numerical Demonstration of the Humidity Effect in Engine Icing," SAE Technical Paper 2019-01-2015, 2019.
https://doi.org/10.4271/2019-01-2015

[59] Ozcer, I. A., Baruzzi, G. S., Reid, T., Habashi, W. G., Fossati, M., and Croce, G., "FENSAP-ICE: Numerical Prediction of Ice Roughness Evolution, and Its Effects on Ice Shapes," SAE Technical Paper 2023-01-1431, 2011.
https://doi.org/10.4271/2011-38-0024

[60] Croce, G., De Candido, E., Habashi, W., Aubé, M., and Baruzzi, G., "FENSAP-ICE: Numerical Prediction of In-Flight Icing Roughness Evolution," *1st AIAA Atmospheric and Space Environments Conference*, AIAA Paper 2009-4126, 2009.
https://doi.org/10.2514/6.2009-4126

[61] Ozcer, I., Norman, A., Moula, G., and Pons, D., "2nd Ice Prediction Workshop Results - FENSAP-ICE v23R2 - ANSYS Canada," *2nd AIAA Ice Prediction Workshop*, 2023, https://folk.ntnu.no/richahan/IPW/files/IPW2/Presentations/IPW2_Presentations/0950_Ozcer_IPW2-Ansys-Vienna.pdf.

[62] Mundo, C., Sommerfeld, M., and Tropea, C., "Droplet-Wall Collisions: Experimental Studies of the Deformation and Breakup Process," *International Journal of Multiphase Flow*, Vol. 21, No. 2, 1995, pp. 151–173.
https://doi.org/10.1016/0301-9322(94)00069-V

[63] Mundo, C., Tropea, C., and Sommerfeld, M., "Numerical and Experimental Investigation of Spray Characteristics in the Vicinity of a Rigid Wall," *Experimental Thermal and Fluid Science*, Vol. 15, No. 3, 1997, pp. 228–237.
https://doi.org/10.1016/S0894-1777(97)00015-0

[64] Honsek, R., and Habashi, W. G., "FENSAP-ICE: Eulerian Modeling of Droplet Impingement in the SLD Regime of Aircraft Icing," *44th AIAA Aerospace Sciences Meeting and Exhibit*, AIAA Paper 2006-0465, 2006.
https://doi.org/10.2514/6.2006-465

[65] Fouladi, H., "Computational Methods for Rotorcraft Icing," Ph.D. Dissertation, Dept. of Mechanical Engineering, McGill Univ., Montreal, QC, Oct. 2015.